Morphologydependent stimulated Raman scattering imaging. I. Theoretical aspects

Pamela M. Aker, Philip A. Moortgat, and JianXiang Zhang

Morphology-dependent stimulated Raman scattering imaging. I. Theoretical aspects

Pamela M. Aker, Philip A. Moortgat, and Jian-Xiang Zhang
Department of Chemistry, University of Pittsburgh, Pittsburgh, Pennsylvania 15260

Morphology-dependent stimulated Raman scattering is a nonlinear laser Raman spectroscopy that relies on using the cavity modes associated with micron-sized structures to enhance optical signal generation. Since different cavity modes occupy different regions in space, location-specific spectra can be generated. Here we outline the physics behind morphology-dependent stimulated Raman scattering imaging and model the signal generation process. The results show that a simple tailoring of the illumination conditions allows signal from single, but selectable, cavity modes to be generated. Thus, this nonlinear Raman technique can be used to image spatial variations in chemical composition and/or molecular structure within microstructures. © *1996 American Institute of Physics.* [S0021-9606(96)01841-7]

I. INTRODUCTION

Morphology-dependent stimulated Raman scattering (MDSRS) is a nonlinear Raman spectroscopy that relies on using the cavity modes associated with small particles to enhance optical signal generation. From a topological standpoint, MDSRS is quite interesting. The cavity modes, called morphology-dependent resonances (MDRs) are located close to the particle surface, and penetrate to a depth only up to a/m, where a is the particle radius and m is the refractive index. What this means is that when an MDSRS spectrum of a liquid droplet, for example, is taken, the data provide information only on molecules located in the droplet outer crust. While this aspect of signal generation bodes ill for experiments that aim to generate information on total droplet chemical content, or study reactions which occur deep in the droplet body, it bodes well for experiments that aim to probe the structure of the droplet/air interface or determine the kinetics of reactions that take place on or near the droplet surface.

The theoretical studies presented here show that the regional character of MDSRS signal generation is even more highly localized than previously thought.[1–3] We show that the MDSRS signal is generated from a narrow ~135-nm-wide annular ring inside a spherical liquid water droplet. The diameter of the annular ring accessed in an experiment can be varied, and as a result the MDSRS signal can be generated at different depths below the liquid water/air surface. This imaging capacity is most unusual and highly opportunistic because MDSRS is not limited exclusively to probing liquid water droplets. Almost any structure can be interrogated; the only proviso is that the material comprising the structure be dielectric in character and the structure be regular (spherical, elliptical, cylindrical, i.e., axisymmetric). The highly localized aspect of MDSRS signal generation opens new avenues in imaging sciences, for it is possible to image molecular structure changes across interfacial chemical systems that span a rainbow of phases (i.e., solid/solid, solid/liquid, liquid/liquid, solid/air, liquid/air) and a diversity of chemical identities (i.e., inorganic nonmetallics, organic polymer blends, and biological membrane systems).

The purpose of this paper is to familiarize the reader with the physics behind MDSRS imaging. We outline the theoretical principles and present model calculations. In an accompanying paper,[4] we provide experimental results which verify that MDSRS can be used to image molecular structure changes across liquid water/air interfaces. We have performed experiments on charged water droplets and have measured the water structure in the diffuse part of the droplet's electric double layer. We have also monitored water response to change in droplet charge. The results of our imaging experiments on the diffuse region of the electric double layer are novel in the sense that this is the first time, to our knowledge, that an experiment has provided information on solvent structure in this region. The knowledge gained by our experiments is not necessarily new, for the behavior we see is that predicted by simple Gouy–Chapman theory. However, this is a positive result for it shows that the MDSRS imaging data can be used directly and that the experiment is not contaminated by artifact.

II. HOW CAVITY MODES ENHANCE AND LOCALIZE RAMAN SIGNAL

Since the time of Mie it has been known that MDRs associated with particles that have regular structure participate in optical scattering (elastic and inelastic) and absorption events.[5–7] The MDRs act to enhance cross sections associated with both linear and nonlinear spectroscopic processes. Here we are concerned with the latter, and specifically we detail the influence that MDRs have on stimulated Raman scattering in aerosols, a process labeled MDSRS.

MDR spectral positions, spatial locations, and lifetimes can be determined using formal Lorenz–Mie scattering theory,[5–24] or other analytic approaches.[25,26] In the following we refer to spheres, but similar formulas are available for other shapes.[27,28] MDRs can be transverse electric (TE) or transverse magnetic (TM), and are characterized by an angu-
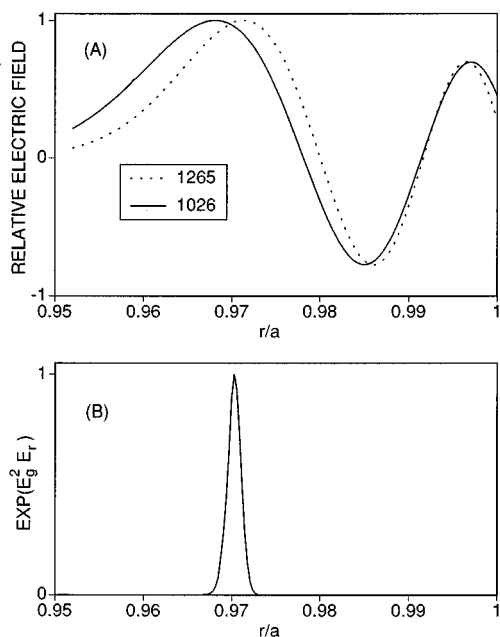
FIG. 1. (A) The electric field distributions of a ''green'' (dotted line, $\lambda=532$ nm, $n=1265$, $l=3$) and a ''red'' (solid line, $\lambda=651.6$ nm, $n=1026$, $l=3$) MDR associated with a water droplet of radius 83.275 μm. (B) The radial MDSRS intensity is proportional to $\exp(E_{green}^{2}E_{red})$. This nonlinearity effectively confines the signal to a narrow annular ring which has a width at FWHM of 135 nm.

lar mode index, n, a radial mode index, l, and an azimuthal mode number $n_m[=\pm n, \pm(n-1),\ldots]$. The MDRs are also characterized by a Q factor, which is a measure of the amount of energy which can be stored in a mode;

$$Q=2\pi c\gamma/m\lambda_{MDR}, \tag{1}$$

where c is the speed of light, γ is the mode lifetime, and λ_{MDR} is the mode wavelength.[10] MDR angular mode numbers can take values between $n=x$ and $n=mx$, where $x=2\pi a/\lambda$, and λ is the wavelength of interest.[10] In principle l can take a value between 1 and $\sim 1.4(n)^{1/2}$, but in practice, modes with $l>50$ have such small Q values that they effectively do not contribute to nonlinear optical signal generation.[20]

MDRs enhance stimulated Raman scattering in two ways. First, when light is coupled into what we refer to as a green (since our $\lambda_{inc}=532$ nm) or pump mode, it remains trapped in the mode volume for the lifetime of the MDR.[1] The net effect of the trapping is to increase the optical path length to $1=c\gamma/m$, i.e., to 2.2 m when $\gamma=10$ ns. The angle-averaged internal electric field distribution of the trapped light is described by a spherical Bessel function, $j_n(mkr)$, where $k=2\pi/\lambda$ and r is the radius. The dotted line in Fig. 1(A) shows the internal electric field of a green MDR with $n=1265$ and $l=3$. Note that electric field peaks approximately at $r_{MDR}\sim(n+1/2)\lambda_{MDR}/2\pi m$ (we will discuss the exact peak position later).[9] At r values smaller than this, $E[j_n(mkr)]\sim 0$, and at larger r the electric field is characterized by a spherical Bessel function of order l (i.e., there are l nodes in the radial intensity distribution).

Second, enhanced Raman scattering in part of the green mode volume occurs whenever there is spatial overlap with a red or Stokes mode (that has $\lambda_{MDR}=\lambda_{Stokes,material}$). The red mode provides a localized electric field which changes the polarization and enhances Raman scattering.[29] The solid line in Fig. 1(A) shows the electric field of a red MDR with $n=1026$, $l=3$. Note that only those molecules found within the red mode volume experience enhanced scattering. This effect, when combined with the exponential dependence of the MDSRS signal on green mode intensity,[1] i.e., $I_{MDSRS}(r)\alpha\exp[E_{green}(r)^2E_{red}(r)]$, enables the measured signal to be assigned to a highly localized region inside the microparticle, a region which we dub as the working volume. This is evident from Fig. 1(B), which shows that $>90\%$ of the MDSRS signal comes from a narrow, ~ 135-nm-wide annular ring. This signal localization phenomenon is unique and suggests that if light can be preferentially coupled into a specific green (pump) MDR, then the experimentally measured signal can be assigned to this mode's working volume.

Once the light in the green mode has been Raman shifted, it can either scatter from the aerosol (i.e., red light does not stay trapped in a green mode) or become trapped (absorbed) in the red mode volume. The ratio between scattering and absorption is dictated by the square of the ratio between the a_n external scattering coefficient associated with the green mode, which is one since red light cannot remain in this mode, and the c_n internal absorption coefficient associated with the red mode. The Raman shifted light that is scattered from the green mode maintains the green mode angular characteristics, i.e., Chen et al.[30] have shown that there are n_{green} angular peaks in the Raman shifted far-field angular intensity distribution, but the red peaks are phase shifted from the green far-field angular peaks. The phase shift arises as a result of the van de Hulst localization principle, i.e., in the far field the red light appears to arise from a point source at $r_{ext}\sim(n_{green}+1/2)\lambda_{red}/2\pi$ which is further from the sphere origin than the green point source which appears to occur at $r_{ext}\sim(n_{green}+1/2)\lambda_{green}/2\pi$.

The preceding discussion shows that MDRs enhance Raman signal generation via two mechanisms. First, the sample path length is increased by the trapping of incident light in a green mode, and second, the Raman transition moment is enhanced when a red mode overlaps the green mode working volume. The preceding discussion also shows that the signal generated in an MDSRS experiment stems exclusively ($>90\%$) from molecules that are located in the green mode working volume. If the experimental illumination geometry is judiciously tailored so that one particular green mode is preferentially excited, the MDSRS signal can be assigned to a specific r_{MDR} within the structure, provided that the identity of the green mode is known. We show below that translation of an incident Gaussian laser beam off one side of a microstructure allows green modes with successively higher n, and therefore successively larger r_{MDR} to be accessed. MDSRS can therefore be used to spatially image structure and compositional changes which occur on traversal from the bulk through the interface of a microparticle. This imaging capacity provides us with a means by which to interro-
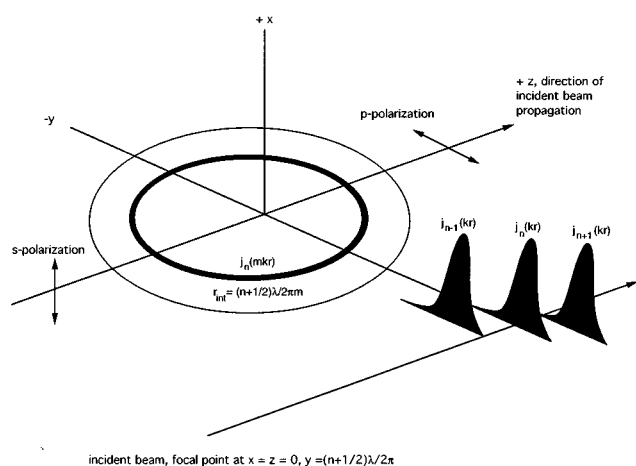
FIG. 2. A pictorial description of the coupling of incident light into a selected aerosol cavity mode. The incident Gaussian laser beam, which is propagating in the $+z$ direction and is s-polarized, is represented as a series expansion of spherical waves. Light couples into the aerosol when the n and λ of a partial wave associated with the incident beam matches the n and λ of an MDR.

gate the substructure of a variety of liquid/gas interfaces and indeed, it provides a means for interrogating hidden interfaces in a variety of liquid/liquid, solid/liquid, and solid/solid systems.

III. SELECTING THE CAVITY MODE

Here we show how preferential excitation of a prespecified green MDR can be effected by tailoring the way a microparticle is illuminated. To start, we note that MDSRS is generated when an incident laser beam is focused off to one side of a particle, with the focal point located up to 35 μm away from the surface. An MDR is excited, even though the light is not directly incident on the particle. Van de Hulst best explains this seemingly anti-intuitive phenomenon with his diffraction based localization principle which states that the spherical partial wave term, $j_n(mkr)$, which describes an MDR with angular mode index n and wave number k ($=2\pi/\lambda$) associated with an aerosol corresponds to a optic ray that passes the aerosol origin at a distance $r \sim (n+1/2)\lambda_{MDR}/2\pi$.[5]

An alternative approach, which is pictured in Fig. 2, is to think of the incident beam as an expanded series of partial waves. Each partial wave is describe by a spherical function $j_n(kr)$ which peaks at $r \sim (n+1/2)\lambda/2\pi$, relative to the origin which is at the center of the scatterer. When the n of $j_n(kr)$ and $j_n(mkr)$ match, the external and internal partial waves angular momentum couple provided that $\lambda_{inc} = \lambda_{MDR}$. The amount of light delivered into the green mode, I_{MDR}, is proportional to the fraction of the incident beam intensity that is partitioned in $j_n(kr)$. In the case where the incident beam is Gaussian in character, the partitioning is determined by the beam waist diameter, which determines the spread in n, and the beam position relative to the center of the scattering sphere, which dictates the magnitude of n.[13–24] Note that as the incident beam is moved to larger r, external $j_n(kr)$

waves with higher n acquire intensity. Thus, green $j_n(mkr)$ modes with higher n are concomitantly excited.

IV. THEORETICAL MODELING OF MDSRS IMAGING

Before we present our modeling results, we briefly describe some pertinent points associated with the experiment. A more extensive description of the apparatus and MDSRS imaging procedure can be found in the accompanying paper.[4] The microdroplets used had radii between 88 and 96 μm (specifiable to 2 parts in 10^5) and were comprised of ultrapure water. UV/vis spectroscopy measurements showed that a Lambert absorption coefficient $\alpha < 0.0005$ cm^{-1} (the instrument limit) characterized both reactant and product aerosol water at 550 nm. The refractive index was measured as 1.331 at 650 nm. We therefore use the wavelength dependent m and k_{im} (where k_{im} is the imaginary component of the refractive index) constants for pure water given by Hale and Querry[31] in the calculations outlined below.

The aerosols were illuminated with the second harmonic of a multimode Nd:YAG (Continuum NY60) laser that has a linewidth of 0.15 cm^{-1} FWHM and a spot size at the point before being focused of 0.6 cm. The incident laser beam was focused onto the droplet equatorial edge with a 20-cm focal length lens, and the spot diameter ($2\omega_0$, defined as the point where the intensity drops to 0.0003 of its on-axis value) at the focus was measured as 89±5 μm. While our laser lases on an average of three modes during each pulse, only the TEM$_{00}$ laser mode will contribute to MDSRS signal generation. Measured temporal, spatial, and spectral beam pulse profiles show that this mode accounts for more than 80% of the incident beam intensity. Since the MDSRS signal scales with $\exp[I_{inc}]$,[1] the signal arising from other transverse modes will be insignificant. In addition, the TEM 01 and 10 modes cannot efficiently couple into the aerosol as their Hermitian spatial distributions at the focal point preclude this. Using $2\omega_0 = (4\lambda/\pi)(F/D)N$, where F is the focal length, D is the incident beam diameter, and N is the number of laser modes, we see that the experimental ω_0 associated with the TEM$_{00}$ mode is 15±1 μm. We also note that the incident intensity was kept low, <2.3 mJ/pulse, in the experiments to prevent saturation of the water MDSRS signal which occurs at pulse energies greater than 8 mJ/pulse.[2,3]

To effect imaging it is necessary that the MDSRS signal be generated from a single green MDR. This is not difficult. To illustrate this, we use the Lorenz–Mie theory to calculate the set of green MDRs associated with an 89.874±0.002 μm radius water droplet ($m = 1.333\,84$, $k_{im} = 1.6657 \times 10^{-9}$ at 532 nm) that can be excited by our Nd:YAG laser. The calculations show that five green modes are present, three are TE, and two are TM. The modes are listed in Table I. They are identified by their n and l mode numbers (all modes have $n_m = 0$) and listed alongside these numbers are the associated wavelengths, peak r_{int} values, and two Q factor values. The first value, Q_{real} is calculated using only the real part of the refractive index; the second value, $Q_{complex}$ is calculated using the complex index of refraction ($m_{complex} = m + ik_{im}$). Before we go further we would like to point out how large and

TABLE I. Green MDRs associated with a water aerosol. $a=89.874\pm0.002$ μm, $m=1.333\,84$.

n	l	λ	r_{MDR}	Q_{real}	$Q_{complex}$	$|d_n|$[a]	$(2n+1)j_n^2(mkr)$
TE 1211	24	532.002	77.453	1.0(43)	4.0(8)	1095	1.247(−2)
TE 1319	8	531.998	84.325	4.6(99)	4.0(8)	1095	1.178(−2)
TE 1396	1	532.003	89.224	2.9(148)	4.0(8)	1095	1.135(−2)
TM 1253	17	532.002	80.089	9.3(68)	4.0(8)	1095	1.214(−2)
TM 1336	6	531.994	85.369	9.5(115)	4.0(8)	1095	1.164(−2)

[a]$|c_n|$ value for TM modes. Values in parentheses denote powers of ten.

completely unrealistic the Q_{real} values are. This happens because theory ignores physical phenomena such as absorption, and refractive index changes that stem from material occlusions, dispersion, and thermal motion. All of these effects serve to degrade the Q factor realized by any structure. While water absorption in the visible region is minuscule, its effect cannot be ignored, as evidenced by the $Q_{complex}$ values. It is worth noting here that several calculations of internal intensity distributions inside aerosols have been presented in the literature, but in most of these cases only the real part of the refractive index was used. The results of these studies should therefore be viewed with caution, as the peak internal intensities calculated this way deviate from those which can be achieved in a real system by many orders of magnitude. Q value calculations which include absorption involve Bessel functions with complex arguments. These functions are time consuming to calculate. Fortunately a simpler formula for estimating the Q value realized in an everyday system is available.[32] It is

$$1/Q = 1/Q_{real} + 1Q_a + 1/Q_{disp} + 1/Q_{reorient},\qquad(2)$$

where $Q_a = m/2k_{im}$, $Q_{disp} = m/\Delta m$, where Δm describes the variation in refractive index over the area spanned by the mode (Δr_{MDR}), or the variation in m over the wavelength range spanned by the MDR (note $Q = \lambda_{MDR}/\Delta\lambda_{MDR}$), and as we have shown previously, $Q_{reorient} = 4\pi^2 ca/\lambda_{MDR}v_{sound}$.[1] The aerosols in our experiments have $Q_a = 4.0\times10^8$ at 532 nm, $Q_{disp}\sim8\times10^{11}$, and $Q_{reorient}\sim1.3\times10^9$, hence all MDR green mode Q values are limited to being $\sim3.5\times10^8$. This upper limit to Q is somewhat detrimental in the sense that it freezes the MDSRS detection limit at $\sim10^{-6}$ M. However, there is a positive outcome to the Q factor absorption limit. It means that all green MDRs associated with our experiments have the same Q. This greatly simplifies the imaging experiment data analysis.

We use the improved Gaussian beam scattering algorithm developed by Lock[20] to determine the amount of energy partitioned into the modes listed in Table I when an incident s-polarized Gaussian 532-nm laser beam is brought in at an arbitrary distance from the droplet center. The Lock theory, which is especially suited for large particles such as we use, shows that the angle averaged internal electric field intensity in each mode is,

$$I(r) = E_0^2/2\Sigma_{nm}\{(2n+1)j_n^2(mkr)|D_n|^2$$
$$+[(n+1)j_{n-1}^2(mkr)+nj_{n+1}^2(mkr)]|C_n|^2\},\qquad(3)$$

where E_0 is the incident unfocused electric field magnitude, $j_n(mkr)$ is the spherical Bessel function of order n, $k=2\pi/\lambda$ is the wave number, r is the internal radius, and

$$|D_n| = B_{n,nm}|d_n|\quad |C_n| = A_{n,nm}|c_n|,\qquad(4)$$

with c_n and d_n the TM and TE Mie internal coefficients calculated for plane wave illumination, respectively, and $A_{n,nm}$ and $B_{n,nm}$ the weighted beam shape coefficients which describe the TM and TE components of the localized incident Gaussian beam, respectively. For an incident s-polarized focused Gaussian beam propagating parallel with the z-axis, with a focal point located at $x_f=0$, $z_f=0$, and $y_f\neq0$ (see Fig. 1), the weighted incident beam coefficients $|A_{n,nm}|$ and $|B_{n,nm}|$ are given by the analytic functions,

$$|A_{n,nm}|\sim\exp[G-(r_f/\omega_0)^2-s^2(n+0.5)^2](2\pi G)^{-1/2}$$
$$\times(n+0.5)^{-nm+1}(2n_m/G)(n)^{nm+1/2},$$

$$|B_{n,nm}|\sim\exp[G-(r_f/\omega_0)^2-s^2(n+0.5)^2](2\pi G)^{-1/2}$$
$$\times(n+0.5)^{nm-1}(2-0.75/G-n_m2/G)(n)^{nm+1/2}.$$
$$(5)$$

Here ω_0 is the Gaussian beam focal waist, $r_f^2=y_f^2+x_f^2$, $s=\lambda/2\pi\omega_0$, and $G=2s(n+0.5)r_f/\omega_0$. The equations for $|A_{n,nm}|$ and $|B_{n,nm}|$ interchange if the beam is p-polarized. We note here that the analytic functions are only valid for $z_f=0$; a different summation must be used in other cases.

Some comments on Eq. (3), which describes the internal intensity distribution, are warranted. We first note that $I(r)$ scales directly with the square of $j_n(mkr)$ since the D_n and C_n coefficients are r independent. The peak of $j_n(mkr)$ thus describes the peak of the internal intensity distribution within a specific MDR. For TE modes an analysis shows that for $n=600$–1500 the spherical Bessel function peaks at $mkr=(0.75\exp[0.3443\ln n]+n+1/2)$, or in other words, the r_{MDR} discussed earlier, which was estimated to peak at $(n+1/2)\lambda/2\pi m$, peaks exactly at $(f+n+1/2)\lambda/2\pi m$, where $f=0.75\exp[0.3443\ln n]$. For the TM modes $f=.606\exp[0.3646\ln n]$. For equivalent n, $\lambda_{TE}>\lambda_{TM}$ (but only by ~0.23 nm), and the result shows that the TE modes peak slightly further out than the TM modes, by about 9 nm.

Another interesting feature of Eq. (3) is that the $(2n+1)j_n^2(mkr_{MDR})$ values (or equivalent for the TM modes) are practically identical for all n. As shown in Table I, the values vary by less than 10% over an n range that spans 1211 to 1396. Table I also shows that the $|c_n|$ and $|d_n|$

Mie plane wave internal coefficients are also independent of n and in fact, are identical for all modes accessible in our experiment. This behavior stems from the fact that our aerosol MDRs have absorption limited Q values. In previous theoretical studies of the relation between MDR linewidth, denoted as $\Delta x_{1/2}$, and the plane wave Mie internal absorption coefficients, it was noted that $\Delta x_{1/2} |d_n|^2 \sim 2$, but that there was a slight increase in the product as a function of n.[9] This relation changes slightly when n is large. For TE modes with $n = 1100$–1500 (and with $m = 1.333\,84$) we calculate that $\ln |d_n|$ (or $\ln |c_n|$ for TM modes)$= -0.501\,19 \ln \Delta x_{1/2} + 0.707\,84$. This relation is assigned with $>99.9\%$ confidence. All green MDRs accessed in our experiment have $\Delta x_{1/2} = 2.67 \times 10^{-6}$, hence their c_n or d_n coefficients are limited to 1095. This is valid when the incident excitation beam is exactly on resonance with the MDR, away from this, the internal coefficient scales as a Lorentzian, i.e.,

$$c_n^2, d_n^2 \alpha \Delta\lambda^2 / [(\lambda_{inc} - \lambda_{MDR})^2 + \Delta\lambda^2], \qquad (6)$$

where $\Delta\lambda = [\Delta\lambda_{MDR}^2 + \Delta\lambda_{inc}^2 + \Delta\lambda_{rad}^2]^{1/2}$. $\Delta\lambda_{MDR}$ is the MDR linewidth (1.74×10^{-6} nm), $\Delta\lambda_{inc}$ is the measured incident laser linewidth (0.0042 nm FWHM), and $\Delta\lambda_{rad}$ is the uncertainty in the MDR wavelength imposed by our ability to specify the droplet radius (measured at two parts in 10^5, $\Delta\lambda_{rad} = 0.0023$ nm).

Since the $(2n+1) j_n^2 (mkr_{MDR})/|d_n|^2$ values do not vary much with n, the relative amount of incident laser intensity partitioned into one particular mode is determined primarily by the $A_{n,nm}$ or $B_{n,nm}$ coefficient associated with the illumination laser beam. As Eq. (5) shows, the $A_{n,nm}$ and $B_{n,nm}$ values are parametrized by the incident beam position (relative to the particle center) and the beam focal spot diameter. A simple tailoring of these two parameters enables input intensity to be preferentially partitioned into one mode, and since the MDSRS signal scales exponentially with I_{MDR}, the experimentally measured MDSRS spectrum can be assigned as arising exclusively from the region encompassed by the selected mode's working volume.

We have calculated the I_{MDR} values (at r_{MDR}), and the fraction of the total MDSRS signal arising from each mode listed in Table I (at r_{MDR}, $f = I_{MDSRS,n}/\Sigma_n I_{MDSRS,n}$) for a series of experimental geometries. Parameters relating to Eqs. (3), (4), and (6) are found in Table I, or listed above in the text. For Eq. (5), which is used to determine the incident beam coefficients, a beam focal waist of 15 μm was assigned, and incident beam positions of $z_f = 0$, $x_f = 0$, and y_f varying from 92 to 122 μm in 10-μm increments were used. The results of our calculations are listed in Table II.

To relate I_{MDR} to absolute MDSRS signal intensity, we use the MDSRS gain equation,

$$I_{MDSRS}(r_{MDR}) = \exp[I_{MDR}(r_{MDR}) A N (d\sigma/d\Omega)$$
$$\times \phi Q_{red}(r_{MDR}) Q_{green}(|a_{green}|/|c_{red}|)^2], \qquad (7)$$

where N is the number density in molec cm^{-3}, $(d\sigma/d\Omega)$ is the Raman cross section, and $A = 16\pi^2 c^3/h\omega_g^2 \omega_s^3 m_s^2$, with g and s referring to the incident and Stokes waves. (Note that

TABLE II. MDR intensity and fractional contribution to total MDSRS signal as a function of incident illumination beam position ($\omega_0 = 15$ μm, $x_f = z_f = 0$, $I_0 = 1.9$ mJ/pulse).

y_f	Mode		I_{MDR}	% of MDSRS Signal
92 μm	TE 1211	$m = 0$	4.18(8)	99.69
		$m = 1$	4.12(8)	0.26
	TE 1319	$m = 0$	3.99(7)	
		$m = 1$	3.94(7)	
	TE 1396	$m = 0$	2.54(6)	
		$m = 1$	2.51(6)	
	TM 1253	$m = 1$	9.79(3)	
	TM 1336	$m = 1$	4.76(2)	
102 μm	TE 1211	$m = 0$	1.02(9)	99.99
		$m = 1$	1.00(9)	
	TE 1319	$m = 0$	4.93(8)	<0.01
		$m = 1$	4.88(8)	
	TE 1396	$m = 0$	1.00(8)	
		$m = 1$	0.99(8)	
	TM 1253	$m = 1$	3.64(4)	
	TM 1336	$m = 1$	6.18(3)	
112 μm	TE 1211	$m = 0$	4.22(8)	
		$m = 1$	4.17(8)	
	TE 1319	$m = 0$	1.04(9)	99.95
		$m = 1$	1.03(9)	
	TE 1396	$m = 0$	6.74(8)	0.05
		$m = 1$	6.67(8)	
	TM 1253	$m = 1$	2.36(4)	
	TM 1336	$m = 1$	1.39(4)	
122 μm	TE 1211	$m = 0$	2.98(7)	
		$m = 1$	2.95(7)	
	TE 1319	$m = 0$	3.74(8)	0.01
		$m = 1$	3.71(8)	
	TE 1396	$m = 0$	7.72(8)	99.98
		$m = 1$	7.65(8)	
	TM 1253	$m = 1$	2.64(3)	
	TM 1336	$m = 1$	5.46(3)	

the A term differs slightly from that previously given,[1] for in the former study it was assumed that light was trapped in a red mode, and not in the green mode as seen here.) As mentioned earlier, there is an enhancement in Raman scattering whenever there is overlap between red and green modes. The enhancement is determined by the red mode's electric field, which is directly proportional to mode Q, i.e., $E_{red}(r_{MDR}) \alpha 2 Q_{red}(r_{MDR})/\omega_{red}$ [here $Q_{red}(r_{MDR}) = j_{red}(mkr_{MDR})/j_{red}(mkr') Q_{red}$, with r' the peak of the red mode electric field, and Q_{red} the absorption limited value], and by the degree of angular ϕ_θ and azimuthal ϕ_ϕ overlap between the red and green mode volumes, i.e., $\phi = \phi_\theta \phi_\phi$. When $r_{MDR,red} \sim r_{MDR,green}$ [i.e., $(n_{red} + 1/2)\lambda_{red} \sim (n_{green} + 1/2)\lambda_{green}$], which is the only case which can give rise to appreciable nonlinear MDSRS signal, the spatial overlap in the angular dimension is $\phi_\theta = [(2n_{red} + 1)/(2n_{green} + 1)]^{1/2}$ and in the azimuthal plane, $\phi_\phi = \exp[-(\phi_{red}/\phi_{green})]$, where $\phi_{red} = \sin^{-1}(n_m/n_{red})$ and $\phi_{green} = \sin^{-1}(n_m/n_{green})$.[19–21] Note that $\phi_\phi = 1$ when $n_m = 0$, and for all other n_m, $\phi_\phi < 0.367$. Lock[20] has recently shown that for the case of equatorial edge illumination (i.e., $\phi_{inc} = 90°$) with an incident Gaussian laser beam, only green modes with $n_m = 0$ to 4 appreciably

couple light into an aerosol, and that the coupling efficiency scales as $n^{(1-nm)}$. In the nonlinear regime we therefore need concern ourselves only with MDRs that have $m_n=0$ and 1 for the signal from the other modes will be minute in comparison. (This is not true when ϕ_{inc} is far from 90°.)

The form of $\phi Q_{red}(r_{MDR})$ is an approximation. A more exact determination of the enhancement in Raman scattering can be made using formal Lorenz–Mie theory, but this calculation is very time consuming when the droplet radius is large, >75 μm). Large order spherical Bessel functions that have large, complex arguments must be computed. While this is not an impossible task, the functions, in the words of Bohren and Huffman,[7] are ''sufficient to make strong men weep.'' We add a note of political correctness here. The Bessel functions are gender neutral; they perturb strong women too. We will present a more exact calculation of the MDR Raman enhancement effect in a future publication.

The calculations were done for scattering at a Raman shift around 3450 cm^{-1}, which corresponds to the OH stretch mode of water. Here the absorption limited Q_{red} is 3.91×10^{7},[31] $(d\sigma/d\Omega)=1.35\times10^{-31}$ cm^2 molec^{-1},[33] $|a_{green}|=1$, since red light is scattered with unit efficiency from a green mode, and $|c_{red}|=436.6$ as determined from the equation relating linewidth and internal absorption coefficient given previously. Red modes with Stokes wavelengths around 651.6 nm were determined by doing Lorenz–Mie calculations for a particle with $a=89.874$ mm and $m=1.331$ (the water refractive index value at 650 nm). Modes which had the best spatial overlap in the green modes' working volumes were identified and used in the signal modeling calculations. Red modes with $n=985$, 1071, and 1135 had optimal overlap with the $n=1211$, 1319, and 1396 green modes, respectively.

The results of our calculations, which are listed in Table II, show that >99.6% of the MDSRS signal stems from *a single mode* at all illumination geometries listed. This is a worst case result. In the calculations we used an E_0 value which corresponded to illumination with 1.9 mJ/pulse incident beam energy. Typical I_0 values of 2.4 mJ/pulse were used in the experiments. The fraction of total MDSRS intensity arising from a particular mode increases dramatically if higher I_0 values are used in the calculations. This point is rather moot, though, for in an experiment, MDSRS spectra measured using incident pulse energies ranging from 1 to 6 mJ/pulse are identical.[3,4] We therefore conclude that spectral differences that might arise if a second mode were concomitantly active (i.e., accounts for up to 5% of the total MDSRS signal) are not discernible within the experimental signal-to-noise.

The results listed in Table II show that TM modes do not generate MDSRS signal. An inspection of Eq. (5) shows that the TM mode $A_{n,nm}$ coefficient is necessarily zero when $n_m=0$. TM modes with $n_m>0$ can be excited by the input beam, but because their $A_{n,nm}$ values are quite small their internal intensities not large enough to allow stimulated Raman scattering to occur, i.e., the gain in these modes is <1. The reverse situation occurs when the incident beam polarization is rotated 90° (i.e., a *p*-polarized incident beam is

used). In this case MDSRS would be generated on TM modes, while signal from TE modes would be suppressed.

Table II shows that the internal intensities associated with TE modes with $n_m=1$ are only slightly smaller than those associated with $n_m=0$ modes but that the MDSRS signal from these modes is small, indeed negligible. This is the result of a spatial overlap effect. As mentioned earlier, modes with $n_m>0$ have ϕ_ϕ values that are at least a factor of $1/e$ smaller than the overlap factor associated with modes with $n_m=0$.

Single mode MDSRS signal generation is not extremely sensitive to input beam position, at least from an experimentalist's perspective. We show this in Fig. 3, which plots the fraction of the total MDSRS signal arising from each mode as a function of incident beam focal point position along the y axis. A careful inspection of this diagram shows that signal from the TE 1211 $n_m=0$ mode dominates the MDSRS output for incident beam positions ranging from 92 to 105 μm. When y_f ranges from 108 to 114 μm, the TE 1319 $n_m=0$ mode accounts for >95% of the signal, and at $y_f>117$ μm MDSRS arises exclusively from the TE 1396 $n_m=0$ mode. This result tells us that small variations in illumination geometry which can result from input laser and aerosol train pointing instabilities (±1 μm and ±1.5 μm, respectively, in our experiment), have little, if any, effect on the signal generation process. It is only in a very small range of y_f that there is the possibility of simultaneously generating MDSRS from two modes. Experimentally this is noticeable. When single mode signal generation occurs, the shot-to-shot MDSRS intensity is stable, and signal fluctuation is determined by the laser shot-to-shot stability. Dual mode excitation causes large intensity fluctuation.

The calculations outlined above have all been done with $x_f=z_f=0$. These positions are also expected to vary slightly in a real experiment. For example, the laser and aerosol train pointing stabilities will influence x_f. We varied x_f by as
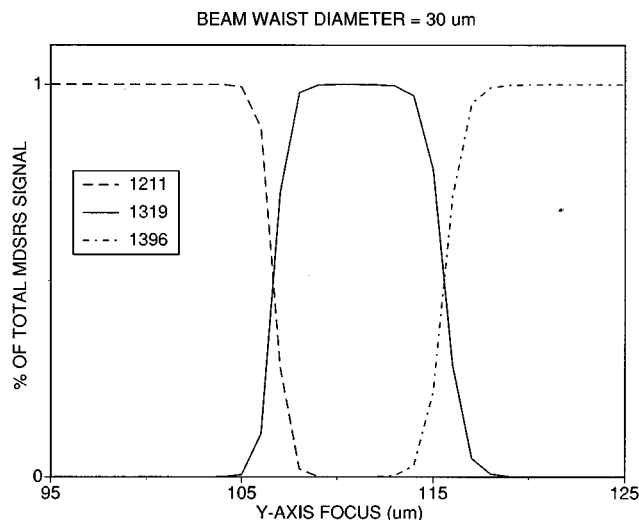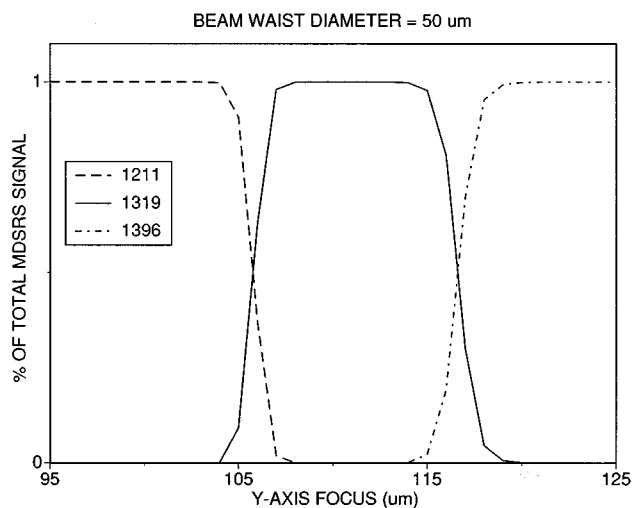

FIG. 3. A plot of the fraction of the MDSRS signal arising in a specific cavity mode as a function of incident illumination geometry. These results were calculated using a beam focal spot diameter of 30 μm.

BEAM WAIST DIAMETER = 50 um

FIG. 4. Results for single cavity mode MDSRS generation for an incident beam focal spot of 50 μm diameter.

much as 7 μm in a separate set of calculations. The results were essentially identical with those listed in Table II and plotted in Fig. 3. Larger variations in the x_f position have a similar effect as shifting the y_f focus, i.e., the $A_{n,nm}$ and $B_{n,nm}$ scale with r_f, where $r_f^2 = x_f^2 + x_f^2$. For example, when $y_f = 102$ μm and $x_f = 0$, MDSRS stems from the TE 1211 mode, but if x_f is 25 μm instead, the signal is exclusive to the TE 1319 mode. Small changes in z_f, < 10 μm, leave the relative I_{MDR} intensity ratios unchanged. The principle effect of moving the focal point along the z axis is to reduce all beam coefficient values, but z_f has to be $\sim 2\omega_0$ in order for any appreciable change in I_{MDR} to be noticed.

Moderate changes in the illumination laser focal beam waist also have minimal impact on the single mode signal generation process. We redid the calculations using $\omega_0 = 25$ μm, a 67% increase in size over that previously given. We have plotted the fraction of total MDSRS signal arising from each mode as a function of incident beam focal point position along the y axis in Fig. 4. The results are almost identical with those shown in Fig. 3.

Our calculations have been done assuming that light contained only in the input laser beam TEM_{00} mode contributes to MDSRS signal generation. Equations (3) and (7) show why this assumption is reasonable. Equation (7) shows that MDSRS signal scales exponentially with I_{MDR} and Eq. (3) shows that this parameter is linearly related to I_{inc} (via the E_0 term) input intensity. The TEM_{00} mode accounts for more than 80% of our total input beam intensity. The small fractions of intensity contained within other modes, such as TEM_{01} and TEM_{10}, are not sufficient to generate stimulated Raman signal. Even if these modes coupled into the aerosol with 100% efficiency, the gain for the nonlinear Raman process remains < 1. The higher transverse modes' Hermitian spatial properties at the focus also preclude them from coupling efficiently into the aerosol. These modes focus at y_f and x_f values that are quite different from the values associ-

ated with the TEM_{00} mode. As a result, their $A_{n,nm}$ and $B_{n,nm}$ values are small.

It might be thought that the large spacing between MDRs would impose limitations on the MDSRS imaging capacity. For example, in the case discussed here, we have shown that MDSRS can be generated in only three widely spaced internal regions, specifically at 12.421, 5.549, and 0.650 μm away from the aerosol surface (corresponding to excitation of the TE 1211, 1319, and 1396 modes, respectively). One would prefer to be able to image structural changes on a much finer spatial grid. However, MDR spectral location is a sensitive function of droplet size and input illumination laser wavelength. For example, a water droplet with radius $a = 89.939$ μm has 3 TE MDRs at 532 nm. These particular modes have $n = 1212, 1320$, and 1397, and can be accessed to generate MDSRS signal at distances 12.422, 5.550, and 0.652 μm from the droplet surface. Another slight change in droplet radius accesses another set of MDRs, each with a different n and each located at a different distance from the surface. Fine spatial grid imaging can therefore be accomplished simply by tailoring the experiment so as allow the droplet radius to be continually varied while keeping the incident beam y_f value fixed. If the structure to be imaged has a fixed radius, different modes can be accessed by varying the input beam wavelength. This arises because the MDR size parameter value, denoted by x, depends on both radius and wavelength, i.e., $x = 2\pi/\lambda$.

In our current experiments we identify and assign the MDSRS signal to specific modes using the procedure just outlined. Uncertainties associated with our experimental x_f, y_f, and z_f (± 2 μm) and aerosol radius (± 0.002 μm) values prevent us from being able to conservatively specify the MDSRS signal location to within $\sim \pm 0.05$ μm. However, the signal location can be assigned with much better precision. This comes about because MDRs enhance both inelastic and elastic scattering processes. If the elastic scattering intensity (or alternatively the total spectrally unresolved inelastic scattering signal) which arises 90° to the incident beam direction is monitored as a function of aerosol radius, an MDR excitation spectrum is obtained. Theory shows that the spacing (Δa) between successive peaks in this type of spectrum is uniquely specified by the n and l values of the MDRs excited. Accurate identification of MDRs can be made by comparing the experimentally measured Δa with that calculated. This has been verified by Chan et al.[34] When the elastic scattering is monitored simultaneous with MDSRS generation, it becomes possible to precisely, and instantaneously, specify the green MDR accessed in the experiment, and identify not only the region inside the aerosol from which the MDSRS signal arises, but also the position of the external laser source, with respect to the aerosol center.

IV. CONCLUSION

We have combined Lorenz–Mie scattering theory with a spherical wave expansion description of an input Gaussian laser beam to show that the MDSRS signal generated in water droplets illuminated by an off-axis incident laser beam

arises from a highly localized area within the particle. In specific, signal is generated in an ~135 nm wide annular ring. The radius of the ring can be changed by changing the illumination geometry, i.e., by translating the incident Gaussian laser beam further off to one side of the droplet. Droplet cavity modes with successively higher n, and hence successively larger r_{MDR}, are accessed and, as such, MDSRS can be used to spatially image structure and compositional changes which occur upon traversal from the bulk through the interface of a liquid droplet.

MDSRS imaging is by no means exclusive to probing water/air interface structure; indeed theory suggests that a wide range of material systems can be scrutinized using this type of spectroscopy. It should be possible to monitor both apparent and hidden interfaces in liquid/gas, liquid/liquid, solid/liquid, solid/solid, and solid/gas systems that span a diverse range of chemical identities. Thus, spatial variations in molecular structure in layered organic polymers, layered inorganic nonmetallic systems, and biological membranes could be determined. However, in practice there may be some limitations in terms of imaging feasibility. While the only theoretical provisos associated with MDSRS imaging are that the material being investigated be dielectric in character and that the microstructure be axisymmetric, differing material optical properties, i.e., absorption, for example, may influence the signal generation process to an extent such that location specific spectra cannot be generated. We are currently studying such effects and will report on this in a future publication.

ACKNOWLEDGMENT

[1] J.-X. Zhang and P. M. Aker, J. Chem. Phys. **99**, 9366 (1993).
[2] J.-X. Zhang, D. Aiello, and P. M. Aker, J. Geophys. Res. **99**, 25 667 (1994).
[3] J.-X. Zhang, D. Aiello, and P. M. Aker, J. Phys. Chem. **99**, 721 (1995).
[4] J.-X. Zhang, P. A. Moortgat, and P. M. Aker, J. Chem. Phys. **105**, 7276 (1996), following paper.
[5] H. C. Van de Hulst, in *Light Scattering by Small Particles* (Dover, New York, 1957).
[6] M. Kerker, in *The Scattering of Light and Other Electromagnetic Radiation* (Academic, New York, 1969).
[7] C. F. Bohren, and D. R. Huffman, in *Absorption and Scattering of Light by Small Particles* (Wiley, New York, 1983).
[8] S. C. Hill, C. K. Rushforth, R. E. Benner, and P. R. Conwell, Appl. Opt. **24**, 2380 (1985).
[9] S. C. Hill, and R. E. Benner, J. Opt. Soc. Am. B **3**, 1509 (1986).
[10] S. C. Hill, and R. E. Benner, in *Optical Effects Associated with Small Particles*, edited by R. K. Chang and P. Barber (World Scientific, Singapore, 1988), Chap. 1.
[11] E. E. M. Khaled, S. C. Hill, P. W. Barber, and D. Q. Chowdhury, Appl. Opt. **9**, 1166 (1992).
[12] E. E. M. Khaled, S. C. Hill, and P. W. Barber, Appl. Opt. **33**, 524 (1994).
[13] G. Grehan, B. Maheu, and G. Gousbet, Appl. Opt. **25**, 3539 (1986).
[14] B. Maheu, G. Grehan, and G. Gousbet, Appl. Opt. **26**, 23 (1987).
[15] G. Gousbet, G. Grehan, and B. Maheu, Appl. Opt. **27**, 4874 (1988).
[16] G. Gousbet, G. Grehan, and B. Maheu, J. Opt. Soc. Am. A **7**, 998 (1990).
[17] J. A. Lock, J. Opt. Soc. Am. A **5**, 2032 (1988).
[18] J. A. Lock, Appl. Opt. **29**, 3180 (1990).
[19] J. A. Lock, J. Opt. Soc. Am. A **10**, 693 (1993).
[20] J. A. Lock, Appl. Opt. **34**, 559 (1995).
[21] E. A. Hovenac, and J. A. Lock, J. Opt. Soc. Am. A **9**, 781 (1992); J. A. Lock, and E. A. Hovenac, Am. J. Phys. **61**, 698 (1993).
[22] J. A. Lock, and E. A. Hovenac, J. Opt. Soc. Am. A **8**, 1541 (1991).
[23] J. P. Barton, D. R. Alexander, and S. A. Schaub, J. Appl. Phys. **64**, 1632 (1988).
[24] J. P. Barton, D. R. Alexander, and S. A. Schaub, J. Appl. Phys. **66**, 2900 (1989).
[25] C. C. Lam, P. T. Leung, and K. Young, J. Opt. Soc. Am. B **9**, 1585 (1992).
[26] S. Schiller, Appl. Opt. **12**, 2181 (1993).
[27] P. Chylek, J. T. Kiehl, M. K. W. Ko, and A. Ashkin, in *Light Scattering by Irregularly Shaped Particles*, edited by D. W. Shuerman (Plenum, New York, 1980), pp. 153–164.
[28] P. W. Barber, and S. C. Hill, in *Light Scattering by Particles: Computational Methods* (World Scientific, Singapore, 1990).
[29] H. Chew, P. J. McNulty, and M. Kerker, Phys. Rev. A **13**, 396 (1976).
[30] G. Chen, W. P. Acker, R. K. Chang, and S. C. Hill, Opt. Lett. **16**, 117 (1991).
[31] G. M. Hale, and M. R. Querry, Appl. Opt. **12** 555 (1973).
[32] B. R. Johnson, J. Opt. Soc. Am. A **10**, 343 (1993).
[33] J. M. Dudik, C. R. Johnson, and S. A. Asher, J. Chem. Phys. **82**, 1732 (1985). The cross in the OH stretch region, i.e., at a 3450-cm^{-1} Raman shift is approximately three times this.
[34] C. K. Chan, R. C. Flagan, and J. H. Seinfeld, Appl. Opt. **30**, 459 (1991).